ORIGINAL PAPER

The evaluation of the electrochemical properties of Co_3O_4 nanopowders synthesized by autocombustion and sol–gel methods

S. Kalpana[1] · Vinay S. Bhat[2] · G. Hegde[3] · T. Niranjana Prabhu[1] · P. N. Anantharamaiah[1]

Abstract

The present investigation involves two synthesis methods, autocombustion (Co_3O_4-AC) and sol–gel (Co_3O_4-SG), for producing nearly spherical-shaped and polygonal shaped nanomaterials of spinel cobalt oxide (Co_3O_4) respectively as electrode materials. TEM image analysis unveiled distinct particle morphologies for the two samples. The Co_3O_4-AC particles exhibited a nearly spherical shape, whereas the Co_3O_4-SG particles displayed a polygonal shape. The phase purity of the Co_3O_4 samples were confirmed via XRD patterns analysis and the crystallite size was calculated to be 44 nm for Co_3O_4-AC and 36 nm for Co_3O_4-SG. The surface area, estimated via BET experiments, of Co_3O_4-AC was found to be 15 m^2/g, while Co_3O_4-SG exhibited a slightly lower surface area of 11 m^2/g. Co_3O_4-AC exhibited a higher specific capacitance (C_s) of 162 F/g at 0.25 A/g, indicating its superior energy storage capability. On the other hand, Co_3O_4-SG shows a C_s of 98 F/g, indicating slightly lower performance compared to Co_3O_4-AC. Both nanomaterials exhibited better stability, with more than 85% capacity retention after 5000 charge–discharge cycles.

Keywords Co_3O_4 · Autocombustion · Sol–gel · CV · GCD · Cycle stability

Introduction

Increase in the population across the world demands the energy for various activity. Sustainable development goals commitment to United Nations by majority of the countries across the world demands renewable energy and related materials for energy storage. This has necessitated researchers to focus on developing materials with better energy storage performance (Berenguer et al. 2016; Khaldakar et al. 2017; Pinky et al. 2015). The physical properties and versatility of complex transition metal oxides, in particular the cobalt oxide has sparked significant research interest, particularly its ability to easily interact with other materials due to its stable spinel structure and *p*-type semiconducting properties. This is attributed to the presence of both Co^{2+} (high-spin divalent) and Co^{3+} (low-spin trivalent) ions, which occupy tetrahedral and octahedral sites, respectively making them suitable for applications such as catalytic, optics, magnetism, and gas sensing (Reena et al. 2020; Shaheen et al. 2020). The spinel structured Co_3O_4 nanomaterials also exhibit corrosion and oxidation resistance, high surface area, and chemical stability (Warsi et al. 2021) along with enhanced surface reduction–oxidation behaviour, magnetic and electronic properties. The specific atomic-level arrangement of the material's surface plays a crucial role in determining its properties and performance in these applications (Ribeiro et al. 2018). Co_3O_4 metal oxide nanomaterials have been prepared via co-precipitataion method which has shown the pseudocapacitance nature enabling them to be used towards energy conversion and storage applications, as a supercapacitor, and electrode material in Li-ion batteries (Vijayanand et al. 2013; Ramsundar et al. 2015).

Kang et al. (2004) prepared Co_3O_4, Ni-Co_3O_4 and Ni-Co_3O_4 composite by changing the time and temperature

✉ T. Niranjana Prabhu
niranjan1975@gmail.com

✉ P. N. Anantharamaiah
anantharamaiah.cy.mp@msruas.ac.in

1 Department of Chemistry, Faculty of Mathematical and Physical Sciences, M. S. Ramaiah University of Applied Sciences, Bangalore 560058, India

2 Centre for Nano-Materials and Displays (CND), B. M. S. College of Engineering, Bull Temple Road, Bangalore 560019, India

3 Department of Chemistry, CHRIST (Deemed to Be University), Hosur RD, Bhavani Nagar, S. G. Palya, Bangalore 560029, India

via physical mixing and mechanical milling. Using these materials, they studied initial coulombic efficacy of anode material for Li-ion battery. Addition of 10 wt% Ni to Co_3O_4 has shown increased coulombic efficiency from 69 to 79% with a 93.4% of retention capacity at 100 cycles and C_s of 700 mAh/g. Ding et al. (2008) synthesised Co_3O_4 nanofibers via electrospinning method at various annealed temperature (500 °C, 600 °C, 700 °C and 750 °C) as an anode material for Li-ion batteries. Co_3O_4 nanofibers annealed at 700 °C shows capacitance of 1336 mAh/g and 55.8% stability after 40 cycles. Jiang et al. (2021) studied electrochemical properties of Co_3O_4/sepiolite composite, by adopting active sepiolite as a template for the synthesis. This template process provides extra capacity as well as controls the growth of Co_3O_4 particles. It shows 1947 mAh/g capacitance at current density of 1 A/g and even after 1000 cycles, it retains 867 mAh/g of capacitance.

In a study conducted by Ullah et al. (2020), the effect of different concentrations of precipitants, namely NaOH and NH_4OH, on the morphological, structural, and magnetic properties of Co_3O_4 nanomaterials was investigated. 1:3 ratio of precursor ($Co(NO_3)_2 \cdot 6H_2O$) to precipitating agents (NaOH and NH_4OH) was used for the synthesis of Co_3O_4 via a low-temperature precipitation method. The variation in precipitants and their concentrations played a significant role in determining the surface morphology of Co_3O_4, as confirmed by FESEM analysis resulting in the enhanced activity for various applications. In another study, Uma Sudharshini et al. (2020) synthesized Co_3O_4 cubic spinel structures with sheet-like morphologies using a solvothermal method at a low-temperature reaction process. The resulting material exhibited a lower ferromagnetic nature but had a high C_s of 778 F/g, which is attributed to its high surface-volume ratio and shorter path length. These characteristics make them suitable as an effective electrode material for supercapacitors. Li et al. (2021) have prepared cost-effective poly-active centric Co_3O_4–CeO_2/Co–N–C composite catalysts with a higher surface area through a facile process for high oxygen evolution reaction (OER) in zinc-air batteries. The composite demonstrated a C_s of 728 mA h/g at 20 mA/cm^2 and exhibited longer stability, thanks to the synergistic effects of the components present in the composite. Hu et al. (2019) have prepared nickel foam, Copper foam, Nickel mesh and Stainless Steel (SLS) mesh as electrocatalysts for oxygen evolution and water splitting reactions in alkaline media. Among these nickel foam & SLS substrate have shown good results with good stability towards oxygen evolution & water splitting applications. Carbon nanomaterial using Acacia auruliformis pods for supercapacitors have been prepared and electrochemical experiments have been conducted by coating these material on the surface of Nickel foam substrate (Bhat et al. 2021), which has shown high performance

towards supercapacitor applications. In a study by Zallouz et al. (2021), Co_3O_4 nanomaterials embedded in mesoporous carbon and subjected to pyrolysis exhibited a C_s of 54 F/g at a current density of 1.0 A/g that exhibited 82% stability over 10,000 cycles. Liao et al. (2015) synthesised Co_3O_4/vertically aligned graphene nanosheets (VAGN)/carbon fabric hybrid composite through a hydrothermal method, which displayed a capacitance of 580 F/g and retention stability of 86.3% over 20,000 cycles, at a high current density of 20 A/g. Additionally, it showed an energy density (E.D.) of 80 Wh/kg and a power density (P.D.) of 20 kW/kg. Li et al. (2016) synthesized Co_3O_4 using a solution process at 70 °C, resulting in a C_s of approximately 304 F/g (C_s) with a 1 M KOH electrolyte solution. However, when Co_3O_4 was combined with super-P-carbon to form a pseudo-supercapacitor, the C_s value increased to around 480 F/g. This Co_3O_4-based nanomaterial demonstrated excellent retention stability of approximately 88.6% over 1000 cycles.

Earlier literature suggests, less attention is given on the studies related to electrochemical performance of materials at lower electrolyte concentrations and lower current density. Hence, this study focuses on the evaluation of electrochemical performance of Co_3O_4 nanomaterials, synthesized by autocombustion and sol–gel methods, at lower electrolyte concentration and lower current density. Different synthesis methods can also lead to different morphology of the particles, which eventually affect the properties of the materials. Herein, Co_3O_4 nanopowders synthesized from two different methods (simple and cost-effective methods) and investigated synthesis method effect on morphology and electrochemical performance of the materials synthesized. For better comparison and correlation, all electrochemical experiments were carriedout under identical conditions. The C_s of the fabricated electrodes was measured to be 162 F/g for Co_3O_4-AC and 98 F/g for Co_3O_4-SG at current density of 0.25 A/g. Furthermore, the prepared nanomaterials exhibited excellent stability, with approximately 100% retention of their performance over 1000 cycles and shows 90% and 88% retention after 5000 cycles for Co_3O_4-AC and Co_3O_4-SG respectively.

Materials and methods

Chemicals

Cobalt nitrate ($Co(NO_3)_2.6H_2O$), tartaric acid and ethylene glycol were procured from SD Fine-Chem Ltd., whereas the glycine (NH_2CH_2COOH) was procured from Avra synthesis Pvt Ltd. All chemicals were employed for synthesis as procured, without further purification.

Synthesis of Co$_3$O$_4$ via autocombustion and sol–gel methods

Figure 1 shows the schematic representation of Co$_3$O$_4$-AC nanomaterial synthesis by autocombustion method. A stoichiometric amounts of Co(NO$_3$)$_2$·6H$_2$O and NH$_2$CH$_2$COOH were dissolved in dis. H$_2$O in a 100 ml crystallizing dish. The reaction mixture was then dehydrated on a hot plate, where the reaction mixture caught fire releasing the brown fumes, resulting in a black-coloured cobalt oxide nanomaterials. The product was then calcinated at 450 °C for 3 h. After cooling, it was ground to fine powder to obtain Co$_3$O$_4$-AC (Salunkhe et al. 2012).

Figure 2 shows the schematic representation of Co$_3$O$_4$-SG nanomaterial synthesis by sol–gel method. A stoichiometric amount of tartaric acid solution (1.0344 g in 30 ml dis.H$_2$O) heated at 50 °C for 30 min with continuous stirring. It is then added with cobalt nitrate solution (2 g in 20 ml of dis.H$_2$O) with stirring. The temperature was increased to 70 °C and maintained for 30 min with continuous stirring. 0.4 ml of ethylene glycol was added drop-wise to the reaction mixture, which resulted in the formation of a light pink coloured gel with the release of brown gas. The resultant product was dried in an oven at 70 °C for 30 min and then dried overnight at 80 °C. The product was cooled and ground to fine powder in a mortar and calcinated in a furnace at 500 °C for 2 h to obtain black coloured Co$_3$O$_4$-SG (Jagtap et al. 2017).

Fig. 1 Schematic representation of Co$_3$O$_4$ nanopowder synthesis via autocombustion method
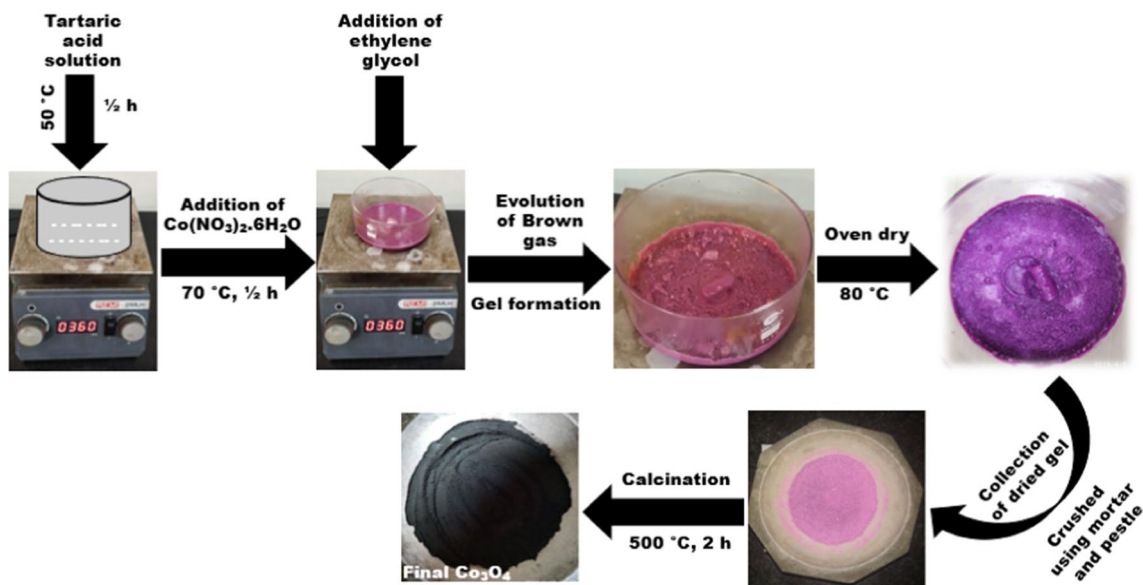

Fig. 2 Schematic representation of Co$_3$O$_4$ nanopowder synthesis via sol–gel method

Characterization

The synthesized Co_3O_4 powders obtained through autocombustion and sol–gel methods were subjected to characterization using various analytical techniques. The phase purity and morphology of the nanomaterials after calcination were examined using X-ray diffraction (XRD) analysis performed on a PANalytical X'pert Pro diffractometer. Transmission electron microscopy (TEM) analysis was conducted using a FEI Tecnai G2 F30 instrument to further investigate the morphology of the samples. To determine the surface area, pore size, and pore diameter of the prepared samples, a BET (Brunauer–Emmett–Teller) analysis was carried out using a Belsorp-mini II instrument from Bel, Japan. X-ray photoelectron spectroscopy (XPS) data of Co_3O_4-AC and Co_3O_4-SG were collected using a Thermo K-Alpha X-ray photoelectron spectrometer to gain insight into the chemical composition and electronic states of the nanomaterials. For electrochemical performance evaluation, a three-electrode system was employed. The working electrode was fabricated using the Co_3O_4-AC and Co_3O_4-SG nanomaterials, a saturated Hg/Hg_2Cl_2 electrode served as the reference electrode, and a Pt rod acted as the auxiliary electrode. The electrochemical performance was investigated in 1 M KOH electrolyte. Cyclic voltammetry (CV) and galvanostatic charge–discharge (GCD) experiments were conducted using a multichannel potentiostat/galvanostat (AUTOLAB M204) to assess the electrochemical behavior of the synthesized nanomaterials.

Specific capacitance (C_s) using GCD curves, Energy Density (E.D.) and Power Density (P.D.) of the samples are calculated using the formulae (Sriram et al. 2021; Alem et al. 2023):

$$C_s = J \times \frac{\Delta t}{\Delta V} \tag{1}$$

where, J is the current density, ΔV is the potential window, Δt is discharge time.

$$E.D. = \frac{1}{2} C_s (\Delta V)^2 \tag{2}$$

$$P.D. = \frac{E.D.}{\Delta t} \tag{3}$$

Fabrication of working electrode cyclic voltammetry (CV) and galvanostatic charge–discharge (GCD) experiments

To prepare the working electrode, a homogeneous paste was created by combining 80% of the prepared nanomaterials (Co$_3$O$_4$-AC and Co$_3$O$_4$-SG), 10% ketjen black, and 10% (PVDF) polyvinylidene fluoride in (NMP) N-methyl-2-pyrrolidone as a solvent. The paste was then coated onto both sides of a pre-cleaned nickel foam substrate measuring 1 cm^2. The coated electrode was dried at 80 °C for approximately 12 h to ensure complete evaporation of the solvent molecules. To further enhance the electrode's integrity and compactness, a pressure of 100 kg/cm^2 was applied by pressing the coated electrode. This process resulted in the formation of the working electrode for further experimentation and analysis.

Results and discussions

TEM (transmission electron microscopy) analysis

Figure 3 depicts the results obtained from TEM analysis of Co_3O_4-AC and Co_3O_4-SG samples. In the Co_3O_4-AC sample image, the predominant particle shape is spherical, with a few exceptions displaying a polygonal morphology (refer to Fig. 3a). On the other hand, the TEM image of the Co_3O_4-SG sample showcases well-defined polygonal particles throughout its composition (refer to Fig. 3d). The variance in particle morphology could be attributed to the contrasting processes involved: the AC method potentially triggers spontaneous combustion, whereas the SG method involves a controlled annealing process. High-resolution TEM images (Fig. 3b, e) provide detailed views of the crystal planes that are exposed. Particle size analysis was performed using Gatan digital micrograph software, and the obtained data was used to generate particle size distribution histograms (Fig. 3c, f). The histograms reveal the distribution of particle sizes within each sample. The average particle size was found to be 28 nm for Co_3O_4-AC and 23 nm for Co_3O_4-SG. Furthermore, the interplanar distance (d) between crystal planes was measured and found to be 0.243 nm for Co_3O_4-AC and 0.269 nm for Co_3O_4-SG, specifically corresponding to the (311) crystal plane.

XRD (X-Ray Diffraction) Analysis

Figure 4 presents X-ray powder patterns obtained for the Co_3O_4 -AC and Co_3O_4 -SG methods. In Fig. 4a, the XRD patterns for Co_3O_4-AC and Co_3O_4-SG are displayed, while Fig. 4b shows an enlarged view of the maximum intense peak (311). The XRD patterns of Co_3O_4-AC and Co_3O_4-SG samples closely match the simulated pattern of Co_3O_4 generated via PCW program. This agreement confirms the phase purity of the prepared nanomaterials, as no impurity peaks are observed. Furthermore, the broad peaks observed in the experimental patterns indicate that the crystallites are nano-sized. The crystallite size was
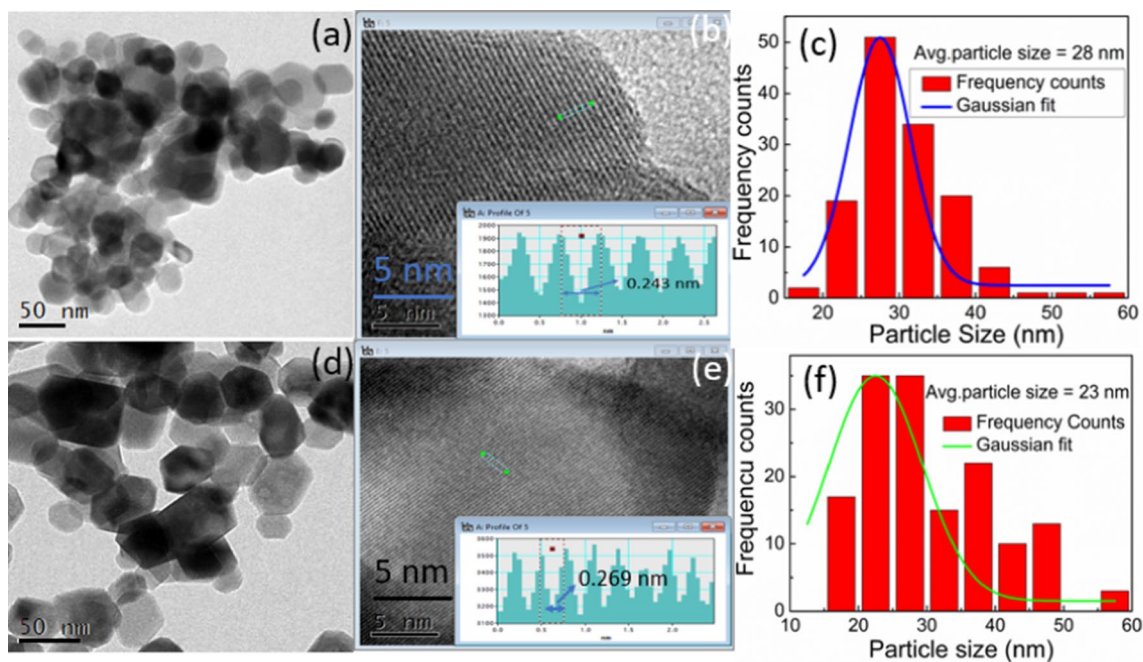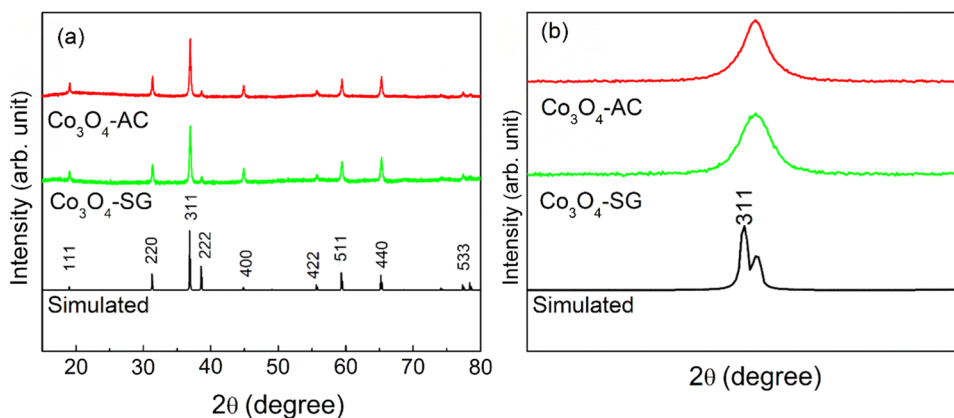
Fig. 3 **a**, **d** TEM images, **b**, **e** HR-TEM, Digital micrograph **c**, **f** corresponding histogram of particle size distribution of Co_3O_4-AC and Co_3O_4-SG samples, respectively

Fig. 4 **a** Observed XRD patterns compared with simulated pattern of Co_3O_4 and **b** enlarged (311) peak of Co_3O_4-AC and Co_3O_4-SG samples

calculated using the Debye–Scherrer formula and found to be 44 nm for Co_3O_4-AC and 36 nm for Co_3O_4-SG. The interplanar distance (d) for (311) plane was calculated using Bragg's law ($n\lambda = 2d\sin\theta$) and determined to be 0.2433 nm for Co_3O_4-AC and 0.2432 nm for Co_3O_4-SG. These values are comparable with the interplanar distances observed in the TEM analysis. The lattice parameter (a) was calculated by relating the (*hkl*) plane to the interplanar distance (d) and found to be 0.8066 nm for both nanomaterials (Chen et al. 2017; Rani et al. 2017).

BET (Brunauer–Emmett–Teller) analysis

Figure 5 presents the N_2 adsorption–desorption isotherms for Co_3O_4-AC (Fig. 5a), Co_3O_4-SG (Fig. 5b) and inset of both figures show the pore size distribution curves respectively. Prior to the analysis, the samples were subjected to a heating process at 120 °C for 3 h to eliminate any moisture or adsorbed gases. The presence of hysteresis loops in the adsorption–desorption isotherms indicates that the prepared samples possess a mesoporous structure. These

Fig. 5 N$_2$ adsorption–desorption isotherms and inset shows pore size distribution curves of **a** Co$_3$O$_4$-AC and **b** Co$_3$O$_4$-SG
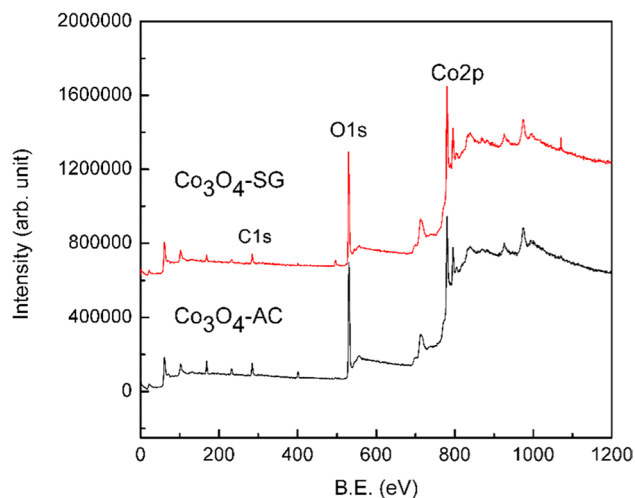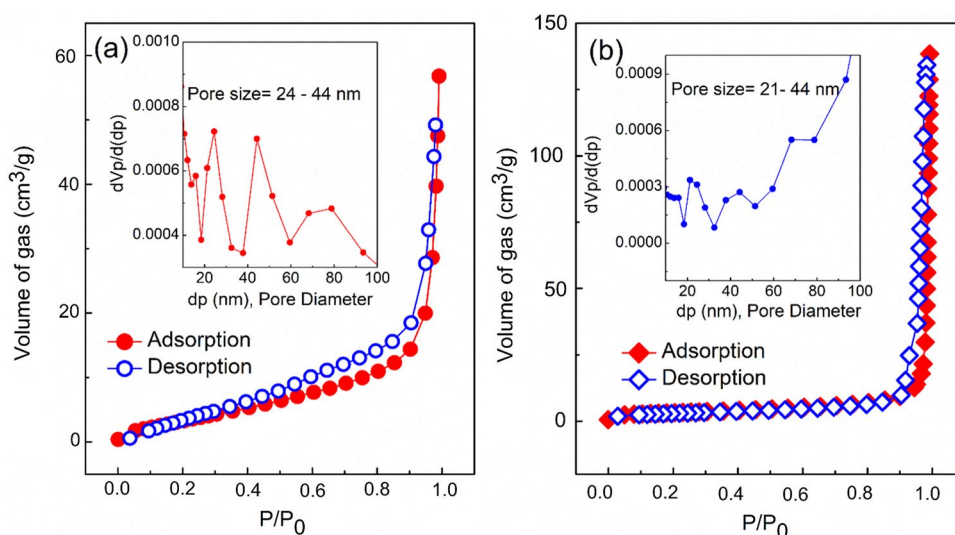

Fig. 6 XPS survey spectra of Co$_3$O$_4$ nanopowders synthesized through sol–gel (SG) and autocombustion (AC) methods

samples follow a type-IV adsorption/desorption isotherm pattern. The surface area, pore volume, and pore diameter of Co$_3$O$_4$-AC were determined to be 15 m^2/g, 0.083 cm^3/g, and 22 nm, respectively. In comparison, Co$_3$O$_4$-SG exhibited higher values for surface area, pore volume, and pore diameter, measuring 11 m^2/g, 0.20 cm^3/g, and 73 nm, respectively. From the pore size distribution curves using the Barrett-Joyner-Halenda (BJH) method, shown in the inset of Fig. 5, it can be observed that both Co$_3$O$_4$-AC and Co$_3$O$_4$-SG samples exhibit a relatively narrow range of pore sizes, specifically ranging from 24 to 44 nm and 21–44 nm, respectively. The determined pore size values for both samples fall within the mesoporous range as reported in previous works (Li et al. 2017; Hitkari et al. 2018; Zhou et al. 2018; Hassanpour et al. 2021). It is important to note that different synthesis methods can lead to variations in surface morphology, thereby affecting the surface area and pore characteristics of the synthesized samples.

X-ray photoelectron spectroscopy (XPS) analysis

Figure 6 illustrate survey spectra of XPS for Co$_3$O$_4$-AC and Co$_3$O$_4$-SG samples, confirming the presence of peaks corresponding to Cobalt (Co) and oxygen (O). In the XPS spectrum of Cobalt (Co), two prominent peaks are observed at binding energies of approximately 780 and 795 eV. These peaks are identified as Co2p$_{3/2}$ and Co2p$_{1/2}$, respectively, (Giri et al. 2022; Tao et al. 2020). Alongside these primary peaks, there are additional satellite peaks with lower intensity. These low intensity satellite peaks can be attributed to the higher Co^{3+} content present in the synthesized samples. (Anantharamaiah et al. 2019; Raj et al. 2019). The binding energies of high-resolution XPS spectra of Co2p and O1s were corrected using a reference carbon (C) binding energy of 284.6 eV and then deconvoluted. The deconvoluted results are presented in Fig. 7.

As depicted in Fig. 7a, the deconvolution of both Co2p$_{3/2}$ and Co2p$_{1/2}$ peaks reveals two distinct components. The component with a lower binding energy corresponds to Co^{3+}, which is situated at the octahedral coordination site. Conversely, the second component corresponds to Co^{2+} and is situated at the tetrahedral coordination site. The binding energies (B.E) of both samples, found after deconvolution, are listed in Table 1, agree well with previous studies (Jang et al. 2017; Zhang et al. 2021). There are no significant changes observed in the binding energies of Co^{2+} and Co^{3+} within both samples. This implies that the samples contain an equivalent quantity of Co^{2+} and Co^{3+} distributed among their respective crystallographic sites.

Figure 7b illustrates the deconvoluted high-resolution O1s spectra for both samples. The primary peak is situated

Fig. 7 Deconvoluted high-resolution XPS spectra of **a** Co2p and **b** O1s for the Co_3O_4 nanopowders made via sol–gel (SG) and autocombustion (AC) methods
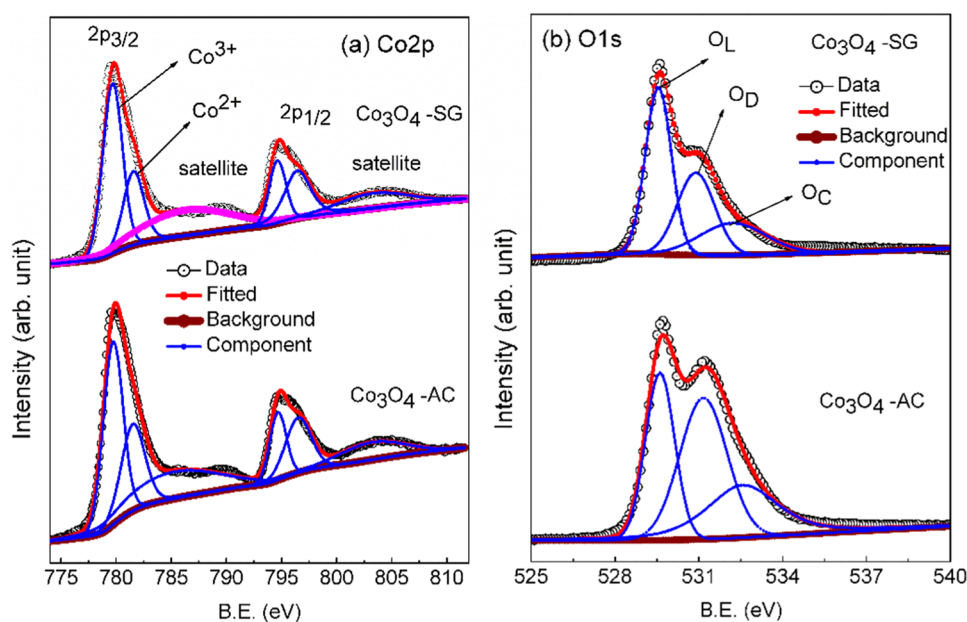

Table 1 List of Co2p binding energies of the samples

Sample	2p$_{3/2}$		2p$_{1/2}$	
	Co^{3+} (eV)	Co^{2+} (eV)	Co^{3+} (eV)	Co^{2+} (eV)
Co_3O_4-AC	779.73	781.52	794.68	796.52
Co_3O_4-SG	779.67	781.57	794.64	796.44

Table 2 List of O1s binding energies of samples

Sample	O$_L$ (eV)	O$_D$ (eV)	O$_C$ (eV)
Co_3O_4-AC	529.61	531.16	532.56
Co_3O_4-SG	529.55	530.89	532.20

at around 529.61 eV and it is accompanied by broadened shoulders at higher B.E. It's worth noting that the shoulder peak's intensity in the Co_3O_4-AC sample is notably greater than what is observed in the Co_3O_4-SG sample. The deconvolution resulted three components: lattice oxygen (O_L), oxygen vacancies (O_V), and chemically adsorbed oxygen (O_C). The binding energies of O_L, O_V, and O_C are approximately 529.6, 531.1, and 532.5 eV, respectively. The O1s B.E values for both samples, as shown in Table 2, align well with existing literature (Ejsmont et al. 2023; Saddeler et al. 2020). This analysis confirms the presence of metal–oxygen (M–O) bonds, specifically Co–O bonding, in both samples.

Cyclic voltammetry (CV)

The CV experiments were conducted for the electrodes, fabricated using Co_3O_4-AC and Co_3O_4-SG nanopowders, at different scan rates such as 5, 10, 25, 50, 75 and 100 mV/s in a three-electrode system using a 1 M KOH electrolyte solution. The obtained CV loops, shown in Fig. 8a,b covered a potential window of 0–0.6 V. Both electrodes exhibited redox behavior characterized by the presence of anodic and cathodic peaks, indicating their pseudo-capacitive nature. Comparison of CV curves of both the samples at scan rate 50 mV/s is shown in Fig. 8c. The first pair of redox peaks (A_1/C_1) can be attributed to the faradaic conversion from Co^{2+} in Co_3O_4 to Co^{3+} (CoOOH), as represented by the equation mentioned previously (Pal et al. 2018; Fan et al. 2019).:

$$Co_3O_4 + OH^- + H_2O \leftrightarrow 3CoOOH + e^- \qquad (4)$$

The second pair of redox peaks (A_2/C_2) observed in the CV curves corresponds to the Faradaic conversion between Co^{3+} (CoOOH) and Co^{4+} (CoO$_2$), as described by the following equation (Liu et al. 2017):

$$CoOOH + OH^- \leftrightarrow CoO_2 + H_2O + e^- \qquad (5)$$
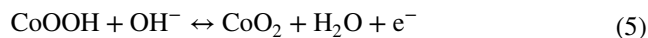
Distinct alterations in the shapes of the CV curves are evident for both electrodes. In the Co_3O_4-AC electrode's case, with rising scan rates, the anodic and cathodic peaks broaden and shift. Conversely, the Co_3O_4-SG electrode exhibits well-defined anodic (A_1 and A_2) and cathodic (C_1 and C_2) peaks, even at higher scan rates, with a minor shift in peak positions compared to the Co_3O_4-AC electrode. The shifting of peaks observed at higher scan rates can be attributed to the influence of polarization effects and the corresponding increase in internal resistance (Li et al. 2020) The CV analysis clearly demonstrates that the Co_3O_4 nanopowders derived from different synthesis

Fig. 8 **a**, **b** CV curves recorded at different scan rates **c** Comparision of CV curves at 50 mV/s and **d** b-values obtained by ploting log(peak current, A) versus log(scan rate, mV/s) of Co$_3$O$_4$-AC and Co$_3$O$_4$-SG samples
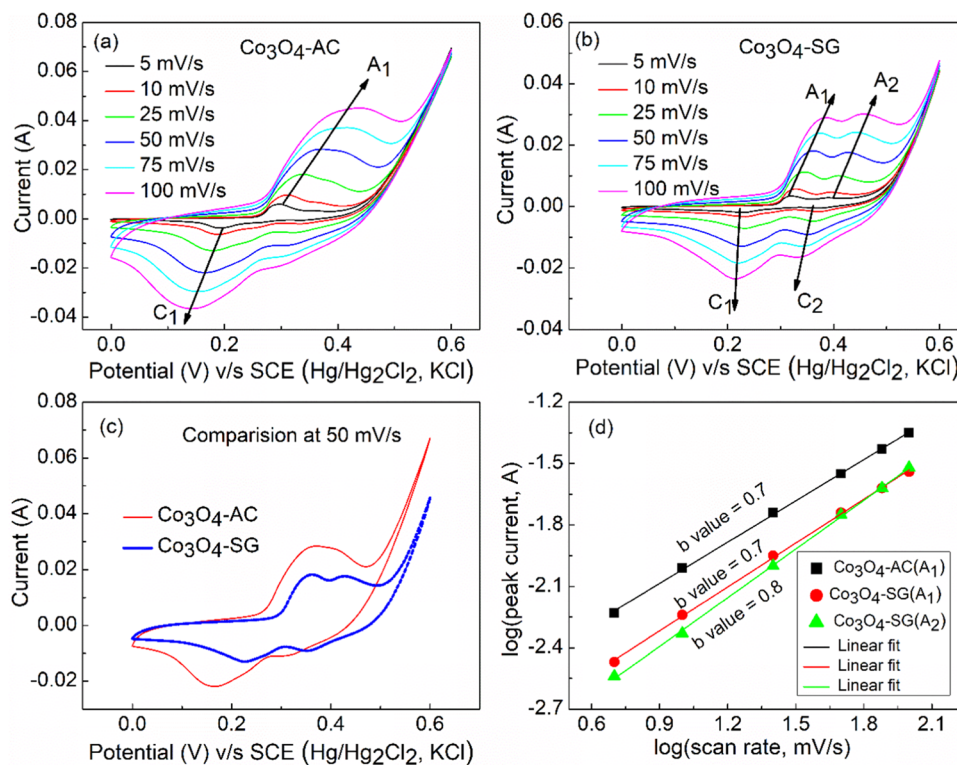
methods exhibit distinct electrochemical behavior, attributable to the differing particle morphologies.

In Fig. 8d, the b-values acquired for the samples are depicted through a plot of log(peak current, A) against log(scan rate, mV/s). Utilizing the power law equation ($i = aV^b$), we deduced the b-values for the fabricated electrodes. Equations (6) and (7) express the logarithmic form of the power law, and Eq. (7) bears resemblance to Eq. (8), which presents a linear relationship (where m signifies the slope corresponding to the b-value, and c represents the intercept). The b-values are derived from the slope of the linear relationship, serving as an indicator of the charge storage behavior of the electrode materials. Here, *i* stands for peak current, *V* denotes scan rate, and *a* and *b* are constant variables. The *b*-value of 0.5 indicates diffusion-controlled behavior, while the *b*-value greater than or equal to 0.7 signifies capacitive behavior of the material. The slopes were determined by performing linear fitting of the log(peak current, A) against log(scan rate, mV/s) data points (Xiong et al. 2021, Chen et al. 2021). The b-values of 0.7 (A$_1$) and 0.8 (A$_1$ and A$_2$) have been calculated for Co$_3$O$_4$-AC and Co$_3$O$_4$-SG respectively. Notably, these b-values lie between 0.5 and 1, indicating that the fabricated electrode materials exhibit a combination of diffusion-controlled and capacitive behaviours. This observation characterizes the synthesized nanomaterials as possessing a pseudo-capacitive nature, analogous to a supercapacitor, (Gao et al. 2018, Guo et al. 2021).

$$\log (i) = \log \left(aV^b \right) \tag{6}$$

$$\log (i) = \log (a) + b\log(V) \tag{7}$$

$$y = mx + c \tag{8}$$

Furthermore, the investigation delved into the charge storage mechanism by assessing the capacitive contribution ratio of the samples through Dunn analysis. Dunn analysis is a method normally employed in electrochemical studies to elucidate and quantify the different charge storage mechanisms occurring in materials, particularly in the context of energy storage devices such as supercapacitors. This technique provides insights into the contributions of capacitive and diffusion-controlled processes to the overall charge storage behavior of a material. The overall current, represented as i(V), results from the combination of capacitive-controlled behavior ($i_c = k_1 v$) and diffusion-controlled behavior ($i_d = k_2 \sqrt{v}$), as derived from Eq. (9). Through subsequent analysis, this relationship was simplified as demonstrated in Eq. (10), resembling the form of Eq. (8) in a linear fashion (Zhang et al. 2019; Babu et al. 2019). The process of determining the values of k_1 and k_2 involves linear fitting of the $i(V)/\sqrt{v}$ versus $\sqrt{v}$ plots, as illustrated in Fig. 9a, b for Co$_3$O$_4$-AC and Co$_3$O$_4$-SG, respectively. This procedure was repeated for different voltage. By obtaining these slope (k_1) and intercept (k_2) values, the respective contribution ratios

Fig. 9 **a**, **b** plots of $i(V)/\sqrt{v}$ versus $\sqrt{v}$ values and **c**,**d** capacitive contribution ratio % (by Dunn analysis) of Co_3O_4-AC and Co_3O_4-SG samples
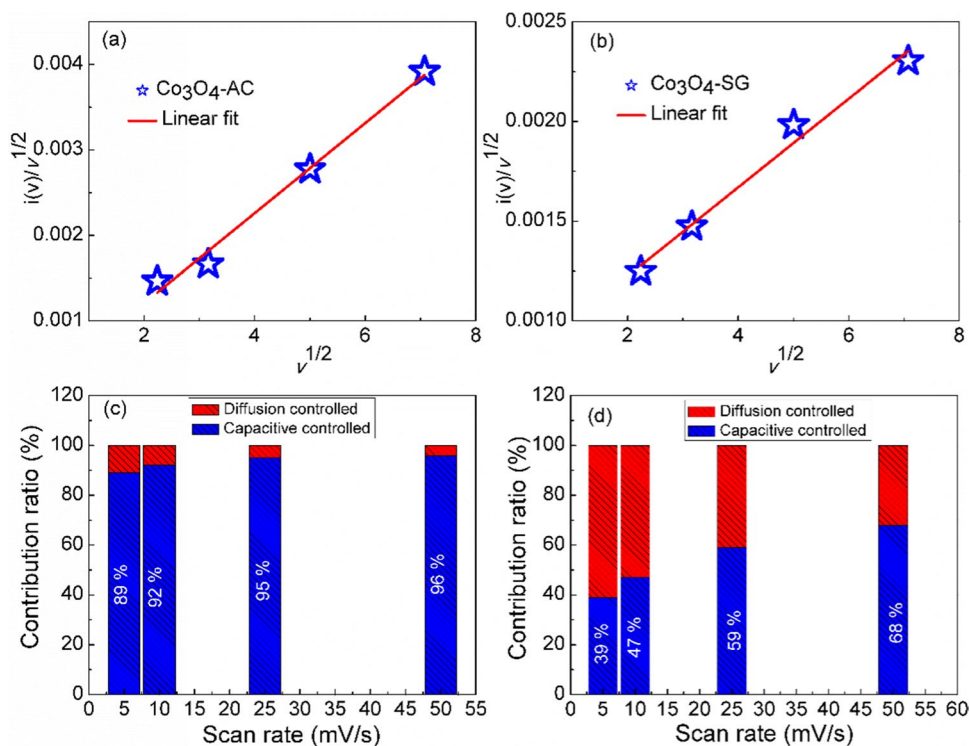
of i_c and i_d were calculated at various scan rates (5, 10, 25, and 50 mV/s). These results are presented in Fig. 9c, d for Co_3O_4-AC and Co_3O_4-SG, respectively. Comparatively, it was observed that Co_3O_4-AC exhibits a higher dominance of capacitive-controlled behavior and a lesser diffusion-controlled behavior as a supercapacitor material in contrast to Co_3O_4-SG material (Iqbal et al. 2021; Ramesh et al. 2021).

$$i(V) = k_1 v + k_2 \sqrt{v} \tag{9}$$

$$\frac{i(V)}{\sqrt{v}} = k_1 \sqrt{v} + k_2 \tag{10}$$

Galvanostatic charge–discharge (GCD)

The GCD curves obtained at various current densities (J) such as 0.25, 0.5, 0.75, 1.0, 2.5 and 5.0 A/g for Co_3O_4-AC and Co_3O_4-SG electrodes are depicted in Fig. 10a, b, respectively. Both samples exhibit two distinct plateaus on the discharging curves, indicating the involvement of redox coupling reactions that were observed in the CV analysis. This behaviour signifies the pseudo-capacitive nature of the materials. Comparing the GCD curves at J of 0.5 A/g (Fig. 10c), it is evident that the Co_3O_4-AC sample displays broader GCD curves compared to the Co_3O_4-SG sample, indicating more charge storage capabilities. This observation is notable considering that Co_3O_4-AC has higher surface

area, pore volume, and pore diameter, as determined in the BET analysis. At a J of 0.25 A/g, the specific capacitance (C_s) values for Co_3O_4-AC and Co_3O_4-SG were measured to be 162 F/g and 98 F/g, respectively. However, as the current density increases, the specific capacitance for both electrodes decreases, as illustrated in Fig. 10d. This decrease can primarily be attributed to the limited interaction between the electrolyte and the active material present on the electrode surface. At all J, the C_s of Co_3O_4-AC is considerably higher than that of the Co_3O_4-SG. Table 3 shows the comparison of specific capacitance of Co_3O_4-AC and Co_3O_4-SG samples with other relevant materials presented in the literature. From the table it is clear that the prepared electrodes show efficacy in retention stability with effective specific capacitance at lower electrolyte concentration and lower current density.

Energy density and power density of Co_3O_4-AC and Co_3O_4-SG electrodes at different current density were calculated and are tabulated in Table 4. The E.D. decreases and the P.D. increases with the increase in current density from 0.25 to 5.0 A/g. Comparatively, Co_3O_4-AC shows relatively higher E.D. than the Co_3O_4-SG nanomaterial.

Electrochemical impedance spectra (EIS)

Figure 11 illustrates the EIS spectra or Nyquist plots obtained for the fabricated Co_3O_4-AC and Co_3O_4-SG nanomaterial electrodes. The EIS spectra exhibit distinct characteristics for both electrode materials. In the higher frequency

Fig. 10 a, **b** GCD curves recorded at different current densities **c** Comparison of GCD curves at current density 0.5 A/g **d** C$_s$ of Co$_3$O$_4$-AC and Co$_3$O$_4$-SG respectively
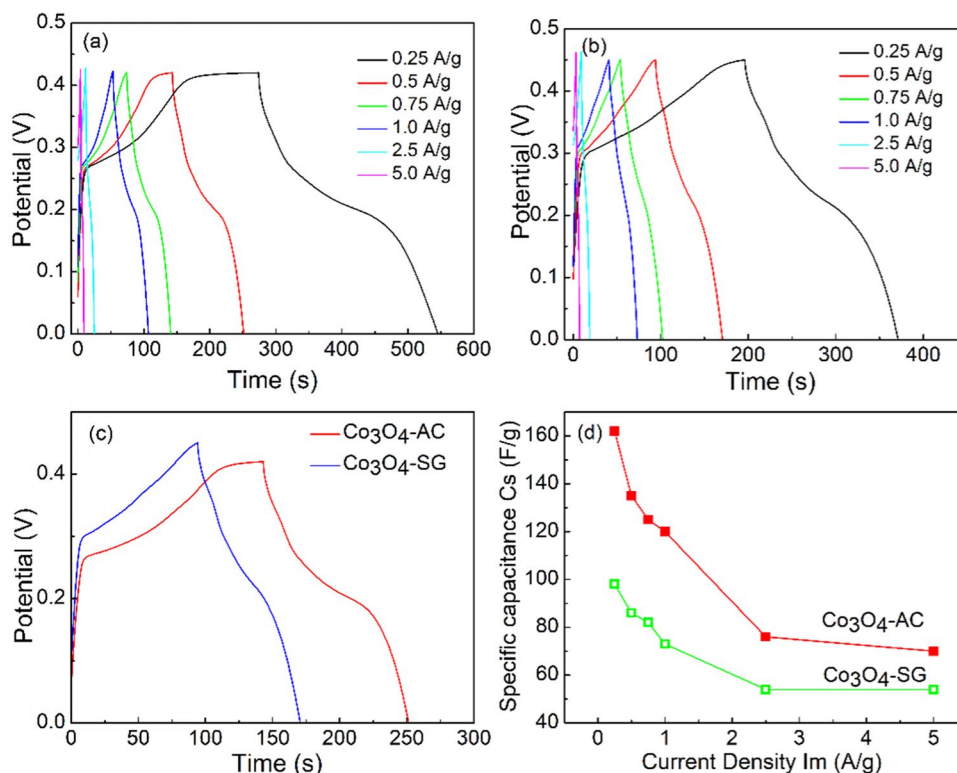

Table 3 Comparison of Specific capacitance of the Co$_3$O$_4$-AC and Co$_3$O$_4$-SG electrodes with the relevant materials reported

Material used	Specific capacitance C$_s$	Current density or scan rate	Retention stability (%)	Number of cycles	Electrolyte used	References
3D Co$_3$O$_4$-Fennel-like	384.375 F/g	3 A/g	96.54	1500	6 M KOH	Li et al. (2017)
Lithiated Co$_3$O$_4$	260 mAh/g	1 A/g	> 92	5000	6 M KOH	Zhang et al. (2020)
Pristine Co$_3$O$_4$	66 mAh/g	1 A/g	< 90	5000	6 M KOH	Zhang et al. (2020)
Zn$_{0.1}$Co$_{2.9}$O$_4$- Spherical	117 F/g	0.1 A/g	–	–	1 M KOH	Kalpana et al. (2023a, b)
Co$_3$O$_4$-Rod shape	261 F/g	0.25 A/g	100	1000	1 M KOH	Kalpana et al. (2023a, b)
5% Ce-doped Co$_3$O$_4$-Nanoflake	1309.86 F/g	5 mV/s	90.86	2000	3 M KOH	Ali et al. (2021)
Undoped Co$_3$O$_4$	942.49 F/g	5 mV/s	76.93	2000	3 M KOH	Ali et al. (2021)
Co$_3$O$_4$-Nanosheet	1455.64 F/g	1 A/g	94.10	2000	3 M KOH	Umar et al. (2021)
Co$_3$O$_4$-tertiary hierarchical (Flower-wire-NM)	254 F/g	0.5 A/g	98.5 (2 A/g)	2000	2 M KOH	Chen et al. (2020)
3D Co$_3$O$_4$ (Electrospinning)	970 F/g	1 A/g	77.5 (6 A/g)	5000	2 M KOH	Lu et al. (2021)
Co$_3$O$_4$-AC	162 F/g	0.25 A/g	90	5000	1 M KOH	Present work
Co$_3$O$_4$-SG	98 F/g	0.25 A/g	88	5000	1 M KOH	Present work

region, a smaller semicircle is observed for the Co$_3$O$_4$-AC electrode, while a larger semicircle is observed for the Co$_3$O$_4$-SG electrode. This difference in semicircle size suggests that the Co$_3$O$_4$-AC electrode has better charge transport properties at the electrode–electrolyte interface compared to the Co$_3$O$_4$-SG electrode. The point of intersection at the

x-axis at the highest applied frequency corresponds to the R$_S$ (Ω) or equivalent series resistance (ESR), which represents the total internal resistance of the cell. The R$_S$ values were found to be 1.42 Ω and 1.16 Ω for the Co$_3$O$_4$-AC and Co$_3$O$_4$-SG electrodes, respectively. The charge transport resistance (R$_{ct}$) of the electrode materials can be estimated

Table 4 E.D. and P.D. values of Co_3O_4-AC and Co_3O_4-SG samples, obtained at different current densities

Current density J (A/g)	Co_3O_4-AC		Co_3O_4-SG	
	E.D (Wh/kg)	P.D (kW/kg)	E.D (Wh/kg)	P.D (kW/kg)
0.25	14.29	0.05	9.92	0.06
0.5	11.91	0.11	8.71	0.11
0.75	11.03	0.16	8.30	0.17
1.0	10.58	0.20	7.39	0.22
2.5	7.03	0.54	5.71	0.57
5.0	6.47	1.08	5.71	1.14
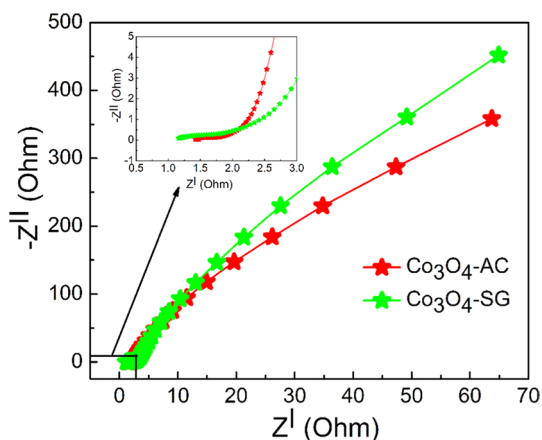
Fig. 11 Nyquist plots for the Co_3O_4-AC and Co_3O_4-SG electrodes. Inset shows the magnified data at high-frequency region

from the radius of the semicircle, which was determined to be 0.92 Ω for Co_3O_4-AC and 2.06 Ω for Co_3O_4-SG. The presence of a vertical line in the low frequency regions indicates the occurrence of ionic diffusion from the bulk of

the solution towards the electrode surface. A more vertical straight line suggests lower diffusive resistance of OH^- ions. The Co_3O_4-AC electrode exhibits a more vertical line in the inset of Fig. 11, demonstrating lower diffusive resistance of OH^- ions from the solution towards the electrode surface. This behavior is consistent with studies conducted by Gaire et al. (2020), Ndambakuwa et al. (2021), Hong et al. (2019), Nieto et al. (2021), Ye et al. (2021), and Kharade et al. (2018).

Stability cycles

The electrode materials' cycle stability was assessed using charge–discharge curves conducted over 5000 cycles under a current density of 5 A/g. The results are depicted in Fig. 12. Both electrodes exhibited nearly identical capacitance retention of 100% up to 1000 cycles. Subsequently, a gradual decline in stability was observed for both electrodes, with Co_3O_4-AC retaining 90% and Co_3O_4-SG retaining 88% stability up to 5000 cycles. This trend of substantial capacitance retention aligns with findings from various cobalt oxide spinel-structured systems, as reported by Sharma et al. (2020), Ghosh et al. (2016), and Thorat et al. (2017).

Conclusions

The successful synthesis of spherical and polygonal cobalt oxide nanomaterials using autocombustion and sol–gel methods has been achieved. X-ray diffraction (XRD) analysis confirms the high phase purity of the nanomaterials, with Co_3O_4-AC having a crystallite size of 44 nm and Co_3O_4-SG with a size of 36 nm. BET analysis reveals that both Co_3O_4-AC and Co_3O_4-SG exhibit mesoporous characteristics, as evidenced by hysteresis loops in N_2 adsorption–desorption isotherms. The surface area, pore volume, and pore
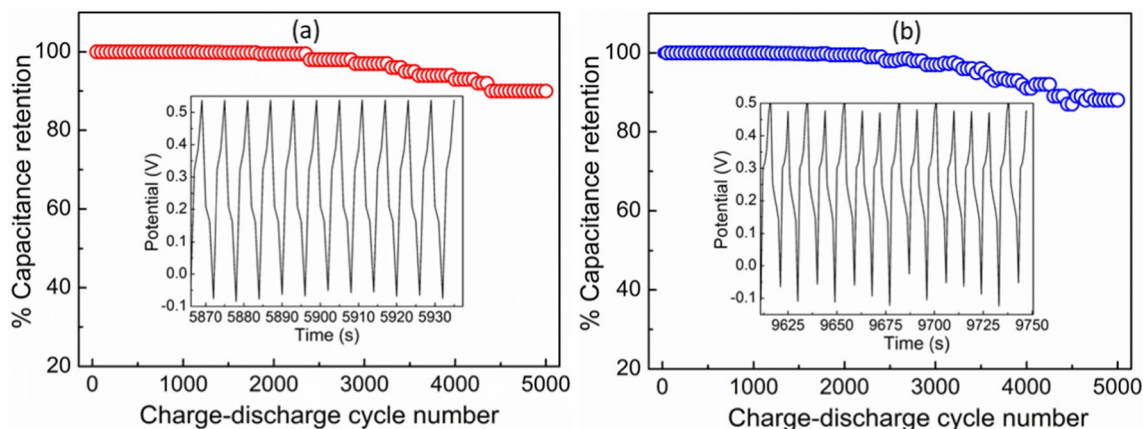
Fig. 12 Stability cycles of **a** Co_3O_4-AC and **b** Co_3O_4-SG samples

diameter of Co_3O_4-AC are determined to be 15 m^2/g, 0.083 cm^3/g, and 22 nm, respectively, while Co_3O_4-SG exhibits values of 11 m^2/g, 0.20 cm^3/g, and 73 nm, respectively. The C_s of Co_3O_4-AC electrode is obtained as 162 F/g, while Co_3O_4-SG exhibits 98 F/g at a current density of 0.25 A/g. As the current density increases, the C_s decreases for both electrodes. Both electrodes exhibited nearly identical capacitance retention of 100% up to 1000 cycles. Subsequently, a gradual decline in stability was observed for both electrodes, with Co_3O_4-AC retaining 90% and Co_3O_4-SG retaining 88% stability up to 5000 cycles.

Declarations

Conflict of interest On behalf of all authors, the corresponding author states that there is no conflict of interest.

References

Alem AF, Worku AK, Ayele DW et al (2023) Ag doped Co_3O_4 nanoparticles for high-performance supercapacitor application. Heliyon 9:e13286. https://doi.org/10.1016/j.heliyon.2023.e13286

Ali F, Khalid NR, Nabi G et al (2021) Hydrothermal synthesis of cerium-doped Co_3O_4 nanoflakes as electrode for supercapacitor application. Int J Energy Res 45:1999–2010. https://doi.org/10.1002/er.5893

Anantharamaiah PN, Joy PA (2019) Effect of co-substitution of Co^{2+} and V^{5+} for Fe^{3+} on the magnetic properties of $CoFe_2O_4$. Phys b Condens Matter 554:107–113. https://doi.org/10.1016/j.physb.2018.11.031

Babu IM, William JJ, Muralidharan G (2019) Ordered mesoporous Co_3O_4/CMC nanoflakes for superior cyclic life and ultra high energy density supercapacitor. Appl Surf Sci 480:371–383. https://doi.org/10.1016/j.apsusc.2019.02.215

Berenguer R, Sieben JM, Quijada C et al (2016) Electrocatalytic degradation of phenol on Pt- and Ru-doped Ti/SnO_2-Sb anodes in an alkaline medium. Appl Catal B 199:394–404. https://doi.org/10.1016/j.apcatb.2016.06.038

Bhat VS, Jayeoye TJ, Rujiralai T et al (2021) Acacia auriculiformis–derived bimodal porous nanocarbons via self-activation for high-performance supercapacitors. Front Energy Res 9:744133. https://doi.org/10.3389/fenrg.2021.744133

Chen H, Lu S, Gong F et al (2017) Stepwise splitting growth and pseudocapacitive properties of hierarchical three-dimensional Co_3O_4 nanobooks. Nanomater 7:81. https://doi.org/10.3390/nano7040081

Chen J, Xu Z, Zhu H et al (2020) An ultrafast supercapacitor built by Co_3O_4 with tertiary hierarchical architecture. Vacuum 174:109219. https://doi.org/10.1016/j.vacuum.2020.109219

Chen F, Chi Y, Zhang H et al (2021) Band-gap shrinked $NiO@Co_3O_4$ nanotubes as high-performance supercapacitor electrodes. J Alloys Compd 888:161463. https://doi.org/10.1016/j.jallcom.2021.161463

Ding Y, Zhang P, Long Z et al (2008) Synthesis and electrochemical properties of Co_3O_4 nanofibers as anode materials for lithium-ion batteries. Mater Lett 62:3410–3412. https://doi.org/10.1016/j.matlet.2008.03.033

Ejsmont A, Kadela K, Grzybek G et al (2023) Speciation of oxygen functional groups on the carbon support controls the electrocatalytic activity of cobalt oxide nanoparticles in the oxygen evolution reaction. ACS Appl Mater Interfaces 15:5148–5160. https://doi.org/10.1021/acsami.2c18403

Fan X, Sun Y, Ohlckers P et al (2019) Porous thin-wall hollow Co_3O_4 spheres for supercapacitors with high rate capability. Appl Sci 9:4672. https://doi.org/10.3390/app9214672

Gaire M, Adireddy BSS, Chrisey D (2020) Ultra-long cycle life and binder-free manganese cobalt oxide supercapacitor electrodes through photonic nanostructuring. RSC Adv 10:40234–40243. https://doi.org/10.1039/D0RA08510C

Gao M, Wang WK, Rong Q et al (2018) Porous ZnO-coated Co_3O_4 nanorod as a high-energy-density supercapacitor material. ACS Appl Mater Interfaces 10:23163–23173. https://doi.org/10.1021/acsami.8b07082

Giri S, Anantharamaiah PN, Sahoo B (2022) Sensing of oxidizing and reducing gases by sensors prepared using nanoscale Co_3O_4 powders: a study through Cu substitution. Adv Powder Technol 33:103529. https://doi.org/10.1016/j.apt.2022.103529

Ghosh D, Lim J, Narayan R (2016) High energy density all solid state asymmetric pseudocapacitors based on free standing reduced graphene oxide-Co_3O_4 composite aerogel electrodes. ACS Appl Mater Interfaces 8:22253–22260. https://doi.org/10.1021/acsami.6b07511

Guo W, Lian X, Tian Y et al (2021) Facile fabrication 1D/2D/3D Co_3O_4 nanostructure in hydrothermal synthesis for enhanced supercapacitor performance. J Energy Storage 38:102586. https://doi.org/10.1016/j.est.2021.102586

Hassanpour M, Niasari MS, Hojaghan HS (2021) Sol–gel synthesis and characterization of Co_3O_4/CeO_2 nanocomposites and its application for photocatalytic discoloration of organic dye from aqueous solutions. Environ Sci Pollut Res 28:7001–7015. https://doi.org/10.1007/s11356-020-11040-3

Hitkari G, Sandhya S, Gajanan P et al (2018) Synthesis of chromium doped cobalt oxide (Cr:Co_3O_4) nanoparticles by co-precipitation method and enhanced photocatalytic properties in the visible region. J Mater Sci Eng 7:2169–2222. https://doi.org/10.4172/2169-0022.1000419

Hong WL, Lin LY (2019) Studying the substrate effects on energy storage abilities of flexible battery supercapacitor hybrids based on nickel cobalt oxide and nickel cobalt oxide@nickel molybdenum oxide. Electrochim Acta 308:83–90. https://doi.org/10.1016/j.electacta.2019.04.023

Hu X, Tian X, Lin YW (2019) Nickel foam and stainless steel mesh as electrocatalysts for hydrogen evolution reaction, oxygen evolution reaction and overall water splitting in alkaline media. RSC Adv 9:31563–31571. https://doi.org/10.1039/C9RA07258F

Iqbal MZ, Zakar SSHS, Alzaid M (2021) Superior performance of cobalt oxide/carbon composite for solid-state supercapattery devices. Phys B Condens Matter 603:412561. https://doi.org/10.1016/j.physb.2020.412561

Jagtap SV, Tale AS, Thakre SD (2017) Synthesis by sol–gel method and characterization of Co_3O_4 nanoparticles. Int J Res Eng Appl Sci 7:1–6

Jang GS, Akhtar SAMS, Kim E (2017) Electrochemical investigations of hydrothermally synthesized porous cobalt oxide (Co_3O_4) nanorods: supercapacitor application. ChemistrySelect 2:8941–8949. https://doi.org/10.1002/slct.201701571

Jiang W, Han Y, Jiang Y et al (2021) Preparation and electrochemical properties of sepiolite supported Co_3O_4 nanoparticles. Appl Clay Sci 203:106020. https://doi.org/10.1016/j.clay.2021.106020

Kalpana S, Prabhu TN, Anantharamaiah PN (2023a) Nanostructured $Zn_{0.1}Co_{2.9}O_4$ material: Synthesis, characterization and its applications for energy storage and electrocatalytic dye degradation. Mater Today Proc. https://doi.org/10.1016/j.matpr.2023.05.590

Kalpana S, Bhat VS, Hegde G et al (2023b) Hydrothermally synthesized mesoporous Co_3O_4 nanorods as effective supercapacitor

material. Inorg Chem Commun 154:110984. https://doi.org/10.1016/j.inoche.2023.110984

Kang YM, Kim KT, Kim JH et al (2004) Electrochemical properties of Co_3O_4, Ni–Co_3O_4 mixture and Ni–Co_3O_4 composite as anode materials for Li ion secondary batteries. J Power Sources 133:252–259. https://doi.org/10.1016/j.jpowsour.2004.02.012

Khaldakar M, Butala D (2017) The synthesis and characterization of metal oxide nanoparticles and its application for photo catalysis. Int J Sci Res 7:499–504

Kharade PM, Thombare JV, Babar AR et al (2018) Electrodeposited nanoflakes like hydrophilic Co_3O_4 as a supercapacitor electrode. J Phys Chem Solids 120:207–210. https://doi.org/10.1016/j.jpcs.2018.04.035

Li G, Mu Y, Huang Z et al (2021) Poly-active centric Co_3O_4–CeO_2/Co–NC composites as superior oxygen reduction catalysts for Zn-air batteries. Sci China Mater 64:73–84. https://doi.org/10.1007/s40843-020-1378-y

Li S, Wang Y, Sun J et al (2020) Hydrothermal synthesis of Fe-doped Co_3O_4 urchin-like microstructures with superior electrochemical performances. J Alloys Compd 821:153507. https://doi.org/10.1016/j.jallcom.2019.153507

Li Y, Hai Z, Hou X et al (2017) Self-assembly of 3D fennel-like Co_3O_4 with thirty-six surfaces for high performance supercapacitor. J Nanomater. https://doi.org/10.1155/2017/1404328

Li ZY, Bui PT, Kwak DH et al (2016) Enhanced electrochemical activity of low temperature solution process synthesized Co_3O_4 nanoparticles for pseudo-supercapacitors applications. Ceram Int 42:1879–1885. https://doi.org/10.1016/j.ceramint.2015.09.155

Liao Q, Li N, Jin S et al (2015) All-solid-state symmetric supercapacitor based on Co_3O_4 nanoparticles on vertically aligned graphene. ACS Nano 9:5310–5317. https://doi.org/10.1021/acsnano.5b00821

Liu F, Su H, Jin L et al (2017) Facile synthesis of ultrafine cobalt oxide nanoparticles for highperformance supercapacitors. J Colloid Interface Sci 505:796–804. https://doi.org/10.1016/j.jcis.2017.06.058

Lu Y, Liu Y, Mo J et al (2021) Construction of hierarchical structure of Co_3O_4 electrode based on electrospinning technique for supercapacitor. J Alloys Compd 853:157271. https://doi.org/10.1016/j.jallcom.2020.157271

Ndambakuwa W, Ndambakuwa Y, Choi J et al (2021) Nanostructured nickel-cobalt oxide and sulfide for applications in supercapacitors and green energy production using waste water. Surf Coat Technol 410:126933. https://doi.org/10.1016/j.surfcoat.2021.126933

Nieto YP, Zaki A, Vidal K et al (2021) Development of $Co_{3-x}Ni_xO_4$ materials for thermochemical energy storage at lower red-ox temperature. Sol Energy Mater Sol Cells 230:111194. https://doi.org/10.1016/j.solmat.2021.111194

Pal B, Krishnan SG, Vijayan BL et al (2018) In situ encapsulation of tin oxide and cobalt oxide composite in porous carbon for high-performance energy storage applications. J Electroanal Chem 817:217–225. https://doi.org/10.1016/j.jelechem.2018.04.019

Pinky SK, Ferdush Ara F, Kurny ASW et al (2015) Photo degradation of industrial dye using ZnO as photo catalyst. Int J Innov Res Sci Eng Technol 4:9986–9992. https://doi.org/10.15680/IJIRSET.2015.0410097

Raj S, Srivastava SK, Kar P et al (2019) In situ growth of Co_3O_4 nano-flakes on reduced graphene oxide-wrapped Ni-foam as high performance asymmetric supercapacitor. Electrochim Acta 302:327–337. https://doi.org/10.1016/j.electacta.2019.02.010

Ramesh S, Karuppasamy K, Sivasamy A et al (2021) Core shell nano-structured of Co_3O_4@RuO_2 assembled on nitrogen-doped graphene sheets electrode for an efficient supercapacitor application. J Alloys Compd 877:160297. https://doi.org/10.1016/j.jallcom.2021.160297

Ramsundar RM, Debgupta J, Pillai VK et al (2015) Co_3O_4 nanorods—efficient non-noble metal electrocatalyst for oxygen evolution at neutral pH. Electrocatalysis 6:331–340. https://doi.org/10.1007/s12678-015-0263-0

Rani BJ, Raj SP, Saravanakumar B et al (2017) Controlled synthesis and electrochemical properties of Ag-doped Co_3O_4 nanorods. Int J Hydrog Energy 42:29666–29671. https://doi.org/10.1016/j.ijhydene.2017.10.051

Reena RS, Aslinjensipriya A, Jose M et al (2020) Investigation on structural, optical and electrical nature of pure and Cr-incorporated cobalt oxide nanoparticles prepared via co-precipitation method for photocatalytic activity of methylene blue dye. J Mater Sci Mater Electron 31:22057–22074. https://doi.org/10.1007/s10854-020-04708-6

Ribeiro RAP, Lazaro SRD, Gracia L et al (2018) Theoretical approach for determining the relation between the morphology and surface magnetism of Co_3O_4. J Magn Magn 453:262–267. https://doi.org/10.1016/j.jmmm.2017.11.025

Saddeler S, Hagemann U, Schulz S (2020) Effect of the size and shape on the electrocatalytic activity of Co_3O_4 nanoparticles in the oxygen evolution reaction. Inorg Chem 59:10013–10024. https://doi.org/10.1021/acs.inorgchem.0c01180

Salunkhe AB, Khot VM, Phadatare MR et al (2012) Combustion synthesis of cobalt ferrite nanoparticles—influence of fuel to oxidizer ratio. J Alloys Compd 514:91–96. https://doi.org/10.1016/j.jallcom.2011.10.094

Shaheen N, Yousuf MA, Shakir I et al (2020) Wet chemical route synthesis of spinel oxide nano-catalysts for photocatalytic applications. Phys B Condens 580:411820. https://doi.org/10.1016/j.physb.2019.411820

Sharma M, Gaur A (2020) Cu doped zinc cobalt oxide based solid-state symmetric supercapacitors: a promising key for high energy density. J Phys Chem C 124:9–16. https://doi.org/10.1021/acs.jpcc.9b08170

Sriram B, Sathiyan A, Wang SF et al (2021) Synergistic effect of Co_3O_4 nanoparticles with Bauhinia vahlii dry fruits derived activated carbon on energy storage applications. J Solid State Chem 295:121931. https://doi.org/10.1016/j.jssc.2020.121931

Tao Y, Wu Y, Chen H et al (2020) Synthesis of amorphous hydroxyl-rich Co_3O_4 for flexible high-rate supercapacitor. J Chem Eng 396:125364. https://doi.org/10.1016/j.cej.2020.125364

Thorat GM, Jadhav HS, Seo JG (2017) Bi-functionality of mesostructured $MnCo_2O_4$ microspheres for supercapacitor and methanol electro-oxidation. Ceram Int 43:2670–2679. https://doi.org/10.1016/j.ceramint.2016.11.081

Ullah AKMA, Amin FB, Hossain A (2020) Tailoring surface morphology and magnetic property by precipitants concentrations dependent synthesis of Co_3O_4 nanoparticles. Ceram Int 46:27892–27896. https://doi.org/10.1016/j.ceramint.2020.07.167

Umar A, Raut SD, Ibrahim AA et al (2021) Perforated Co_3O_4 nanosheets as high-performing supercapacitor material. Electrochim Acta 389:138661. https://doi.org/10.1016/j.electacta.2021.138661

UmaSudharshini A, Bououdina M, Venkateshwarlu M et al (2020) Low temperature solvothermal synthesis of pristine Co_3O_4 nanoparticles as potential supercapacitor. Surf Interfaces 19:100535. https://doi.org/10.1016/j.surfin.2020.100535

Vijayanand S, Kannan R, Potdar HS et al (2013) Porous Co_3O_4 nanorods as superior electrode material for supercapacitors and rechargeable Li-ion batteries. J Appl Electrochem 43:995–1003. https://doi.org/10.1007/s10800-013-0593-7

Warsi MF, Shaheen N, Sarwar MI et al (2021) A comparative study on photocatalytic activities of various transition metal oxides nanoparticles synthesized by wet chemical route. Desalin 211:181–195. https://doi.org/10.5004/dwt.2021.26463

Xiong S, Weng S, Tang Y et al (2021) Mo-doped Co_3O_4 ultrathin nanosheet arrays anchored on nickel foam as a bi-functional electrode for supercapacitor and overall water splitting. J Colloid Interface Sci 602:355–366. https://doi.org/10.1016/j.jcis.2021.06.019

Ye J, Zhai X, Chen L et al (2021) Oxygen vacancies enriched nickel cobalt based nanoflower cathodes: mechanism and application of the enhanced energy storage. J Energy Chem 62:252–261. https://doi.org/10.1016/j.jechem.2021.03.030

Zallouz S, Rety B, Vidal L et al (2021) Co_3O_4 nanoparticles embedded in mesoporous carbon for supercapacitor applications. ACS Appl Nano Mater 4:5022–5037. https://doi.org/10.1021/acsanm.1c00522

Zhang J, Xu Q, Wang J et al (2021) Dual-defective Co_3O_4 nanoarrays enrich target intermediates and promise high-efficient overall water splitting. Chem Eng J 424:130328. https://doi.org/10.1016/j.cej.2021.130328

Zhang M, Fan H, Ren X et al (2019) Study of pseudocapacitive contribution to superior energy storage of 3D heterostructure $CoWO_4$/Co_3O_4 nanocone arrays. J Power Sources 418:202–210. https://doi.org/10.1016/j.jpowsour.2019.02.041

Zhang Y, Hu Y, Wang Z et al (2020) Lithiation-induced vacancy engineering of Co_3O_4 with improved faradic reactivity for high-performance supercapacitor. Adv Funct Mater 30:2004172. https://doi.org/10.1002/adfm.202004172

Zhou R, Chen Y, Fu Y et al (2018) Dandelion-like mesoporous Co_3O_4 as anode materials for lithium ion batteries. Ionics 24:1595–1602. https://doi.org/10.1007/s11581-017-2329-x